PAPER

Check for updates

Understanding the barocaloric response of choline-based hybrid ionic plastic crystals [choline]$_2$CoCl$_4$ and [choline]$_2$ZnCl$_4$

Joshua J. B. Levinsky, [†a] Shivani Grover, [†a] Phillippa Partridge,[a]
Eliza K. Dempsey,[a] Emmanouil K. Charkiolakis,[b] David Gracia,[b]
Marco Evangelisti,[b] Charles J. McMonagle[c] and Claire L. Hobday [*a]

Traditional refrigeration methods based on vapour compression are environmentally damaging, prompting a need for greener alternatives. Hybrid ionic plastic crystals that exhibit order–disorder structural phase transitions around room temperature with large pressure-driven entropy and temperature changes have been identified as viable solid-state refrigerants. The characteristic dynamic disorder of plastic crystals complicates experimental structural probes and requires molecular dynamics simulations to gain insight into the disorder. However, the dynamics of the disordered phase are seldom unambiguously characterized and rarely linked to how they drive the phase transition. In this work, we investigate the barocaloric properties of choline-based plastic crystals [choline]$_2$CoCl$_4$ and [choline]$_2$ZnCl$_4$. Through comprehensive characterization *via* variable pressure–temperature diffraction and *ab initio* molecular dynamics simulations we show that the microscopic mechanism for the observed crystallographic disorder and entropy changes can be attributed to hydrogen bonding competition in the disordered orthorhombic ($Pmcn$) and ordered monoclinic ($P2_1/c$) phases. Our study illustrates the potential of choline-based plastic crystals as viable candidates for barocaloric refrigeration and shows that the combination of theoretical and experimental approaches presented here provides a comprehensive insight into the structural dynamics that drive competitive reversible adiabatic temperature and entropy changes at low working pressures.

1 Introduction

The currently ubiquitous vapour-compression method of refrigeration has a significant downside, namely its reliance on volatile refrigerants with large global warming potentials.[1] In order to overcome this challenge, alternative solid-state refrigerants which exhibit similarly large entropy and temperature changes by the application of external stimuli, the so-called solid-state caloric effects, have to be identified. An all solid-state approach avoids the need for volatile refrigerants with large global warming potentials and promises a higher thermodynamic efficiency.[2] The caloric effects are generally classified by their driving fields into four types: barocaloric (hydrostatic pressure), elastocaloric (uniaxial stress), magnetocaloric (magnetic field), and electrocaloric (electric field). These effects can also be combined in multicaloric materials to achieve enhanced or synergistic responses.[3,4] Magnetocalorics typically exhibit entropy changes of 10–40 J K^{-1} kg^{-1} and often require large applied fields created by superconducting magnets.[5] Electrocalorics have shown large promise in thin films but suffer from their difficulty to scale.[6] Elastocalorics are known to exhibit large caloric responses but suffer from mechanical fatigue.[7] Barocaloric effects stand out for their exceptionally large entropy changes driven by pressure-induced phase transitions in bulk materials that can couple to other order parameters such as magnetic or polar degrees of freedom.[8,9] Thus far, colossal barocaloric effects ($\Delta S \geq 100$ J K^{-1} kg^{-1}) on par with commercial hydrofluorocarbon refrigerants such as R134a where $\Delta S = 520$ J K^{-1} kg^{-1} [10] have been observed in solid–solid phase transitions for a variety of systems such as molecular and (hybrid) ionic plastic crystals,[11–19] two-dimensional perovskites,[20,21] spin-crossover compounds[22–24] and inorganic salts.[25] The exceptionally large barocaloric response found in plastic crystals originates from structural phase transitions from an orientationally disordered state to an ordered state,[26] characterized by a large isothermal entropy change, ΔS_{it}, and large barocaloric coefficient, dT/dP.

[a]*EaStCHEM School of Chemistry and Centre for Science at Extreme Conditions, University of Edinburgh, David Brewster Rd, Edinburgh, EH9 3FJ, UK. E-mail: Claire.Hobday@ed.ac.uk*

[b]*Instituto de Nanociencia y Materiales de Aragón (INMA), CSIC-Universidad de Zaragoza, Zaragoza, 50009, Spain*

[c]*Swiss–Norwegian Beamlines, European Synchrotron Radiation Facility, 71 Avenue des Martyrs, Grenoble, 38000, France*

† These authors contributed equally to this work.

Hydrogen bonding is an important tool in crystal engineering enabling control of inter- or intramolecular interactions and plays a critical role in the physical properties of many technologically important material systems such as the stability and optoelectronic properties of hybrid perovskites.[27,28] In the context of barocalorics, hydrogen bonding has previously been found to play a central role in the order-disorder structural phase transitions observed in molecular plastic crystals.[29] For instance, in a combined computational and spectroscopic study conducted by Li *et al.* on neopentyl glycol, it was demonstrated that hydrogen bonds provide stability to the low-temperature (LT) ordered phase.[29] For molecular plastic crystals more generally, the transition temperature, T_c, increases with increasing number of hydroxyl groups and therefore increases with the possible hydrogen bond pathways.[29]

To further our understanding of the influence of hydrogen bonding in order-disorder phase transitions in plastic crystals and to have control over its barocaloric properties, in this work we combine the hydrogen bond donor choline with metal halide hydrogen bond acceptors. The metal halide anions of choice in this work are $CoCl_4^{2-}$ and $ZnCl_4^{2-}$ which form highly symmetric tetrahedral complexes that promote plastic crystal phase formation. Halometallate anions can function as chemically tuneable hydrogen bond acceptors through selection of the metal centers and halogen. Choline ($C_5H_{14}NO^+$) is a quaternary ammonium ion that readily forms plastic crystalline salts with a variety of counterions due to its globular shape.[30] From a sustainable materials design perspective, choline is an ideal cation due to its non-toxic nature (essential human nutrient[31]) and ability to function as hydrogen bond donor. Ionic plastic crystals (IPCs) have thus far been explored mostly as solid-state electrolytes due to the large ionic conductivity of the plastic crystalline phase.[32] In this work, we seek to understand the barocaloric and structural properties of [choline]$_2$CoCl$_4$ and [choline]$_2$ZnCl$_4$, which are new additions to the broader families of hybrid inorganic–organic IPCs and choline metal halide compounds. Thus far, several choline metal halides compounds such as [choline]FeCl$_4$,[30] [choline]$_3$[CuCl$_4$][Cl],[33] [choline]$_4$[Cu$_4$Cl$_{10}$O][33] and [choline][SnCl$_3$][34] have been reported. However, it is apparent that the reported crystal structures for the known choline metal halide compounds, as well as for plastic crystals in general, suffer from the presence of disorder leading to either incomplete descriptions of the crystal structures[33] or the inability to model the structure all together.[17,19,30,35,36] Furthermore, for choline metal halide compounds, with the exception of [choline]FeCl$_4$, no structural phase transitions are reported for these suspected plastic crystals. In this work, we present thorough structural analyses of the phase behavior of choline-based metal halide plastic crystals.

X-ray diffraction techniques are inherently limited in their ability to probe the fine details of the orientational disorder and dynamic nature of the plastic crystalline phase due to the spatial- and time-averaged crystallographic models they produce. Consequently, for plastic crystals computational approaches such as *ab initio* molecular dynamics (MD) have long been required to gain the atomistic insight needed to rationalize their observed physical properties. Over the years, the increase in available computational power has enabled the simulation of increasingly complex systems which exhibit plastic crystalline phases, from the earliest examples of MD simulations on simple systems such as methane,[37] SF$_6$[38] and CCl$_4$[39] to the hybrid inorganic–organic choline metal halide compounds presented here.

Classical MD has been shown to be a successful approach for modelling the structural dynamics and estimating the thermodynamic properties for a variety of organic ionic plastic crystals[40–45] and promising barocaloric materials such as neopentyl glycol[46] and methylammonium PbI$_3$.[47] However, dynamic disorder in these systems is still usually characterized in terms of the broadening of radial distribution functions[40–42] or the rapid decay of angular autocorrelation functions.[46] As such, the modes driving the order–disorder phase transition and are characteristic of the plastic crystalline phase are rarely identified. Additionally, for the choline-based plastic crystals presented in this work, force fields that accurately describe the intermolecular interactions are not available in literature. This limitation motivates the use of the more rigorous approach of *ab initio* molecular dynamics in the present work. As *ab initio* MD accounts for the temperature and anharmonic effects characteristic to plastic crystals, they are a powerful tool in estimating key thermodynamic quantities, *i.e.* temperature-dependent vibrational frequencies, entropy and free energies.[47,48] Although *ab initio* MD calculations are much more computationally expensive than static DFT or classical molecular dynamics, they are an essential choice of methodology for the present work.

In this work, we present a comprehensive study of the barocaloric properties of [choline]$_2$MCl$_4$ (M = Co, Zn). Combining pressure- and temperature-variable calorimetry and X-ray diffraction experiments with *ab initio* MD simulations provides an in-depth understanding of the atomic origins of the order-disorder structural phase transition and the resulting changes in entropy and temperature. Across the order-disorder phase transition, both [choline]$_2$CoCl$_4$ and [choline]$_2$ZnCl$_4$ exhibit a maximum reversible isothermal entropy change, $\Delta S_{it,rev}$, of 139 J kg^{-1} K^{-1} and 128 J kg^{-1} K^{-1} respectively for a change in pressure, ΔP, of 100 MPa. Additionally, [choline]$_2$CoCl$_4$ and [choline]$_2$ZnCl$_4$ show a maximum reversible adiabatic temperature change, $\Delta T_{ad,rev}$, of 6.1 K for ΔP = 100 MPa. *Ab initio* MD simulations reveal that distinct dynamic behavior characterizes both the monoclinic and orthorhombic phases. The results from the MD simulations agree well with, and inform, the crystallographic models obtained from single crystal X-ray diffraction experiments. We further provide an atomic mechanism to rationalize the observed crystallographic disorder and the large change in isothermal entropy.

2 Methodology

2.1 Experiments

2.1.1 Synthesis. For the synthesis of [choline]$_2$CoCl$_4$ and [choline]$_2$ZnCl$_4$, choline chloride (2 mmol, 0.2792 g, Toku-e) was dissolved alongside CoCl$_2$·6H$_2$O (1 mmol, 0.2379 g, Sigma-Aldrich, reagent grade) or ZnCl$_2$·6H$_2$O (1 mmol,

0.2379 g, Sigma-Aldrich, reagent grade) in 98% ethanol heated to its boiling point. Millimeter-sized blue needle-like single crystals of [choline]$_2$CoCl$_4$ and millimeter-sized white needle-like single crystals of [choline]$_2$ZnCl$_4$ were obtained by slow cooling.

2.1.2 Heat capacity. Heat capacity measurements were conducted using an AK-6-25 adiabatic calorimeter, manufactured by AOZT Termis which provide an accuracy of 0.3%.[49] The experimental data were recorded under ambient pressure conditions in the temperature range from 250 to 350 K, on bulk powder samples of [choline]$_2$CoCl$_4$ (55.7 mg) and [choline]$_2$ZnCl$_4$ (143.2 mg).

2.1.3 Variable-pressure differential scanning calorimetry. Variable-pressure differential scanning calorimetry measurements were performed on a rough powder (consisting of hundreds of as-grown single crystals) of [choline]$_2$CoCl$_4$ (24.9 mg) and [choline]$_2$ZnCl$_4$ (11.8 mg) using a Seteram Microcalvet calorimeter equipped with Hastelloy high-pressure cells. Isobaric heat flow measurements were performed between atmospheric pressure and 100 MPa in 10 MPa pressure steps using a heating and cooling rate of 1 K min^{-1} and N$_2$ gas was used as the pressure transmitting medium. N$_2$ pressures up to 100 MPa were generated using a Teledyne Isco syringe pump.

2.1.4 Calculation of isobaric entropy changes. The isobaric entropy changes, ΔS_{ib}, were calculated by integrating over the peaks observed in the heat flow measurements[50] after the subtraction of a linear background:

$$\Delta S_{ib} = \int_{T_i}^{T_f} \frac{1}{T} \frac{Q(T,P)}{\dot{T}} dT \tag{1}$$

Here, $Q(T, P)$ is the isobaric heat flow signal, T_i and T_f correspond the initial and final temperature of a temperature range near the transition peak, $\dot{T}$ is the scan rate used during the measurement and T is the temperature. The contribution from the heat capacity to the isobaric entropy change, S_{c_p}, was calculated through the following equation:[21]

$$S_{c_p}(T) = \begin{cases} S_{c_p}(T_0) + \int_{T_0}^{T} \frac{c_p^{LT}}{T'} dT' & T_0 \leq T \leq T_i \\ S_{c_p}(T_i) + \int_{T_i}^{T} \frac{c_p}{T'} dT' & T_i \leq T \leq T_f \\ S_{c_p}(T_f) + \int_{T_f}^{T} \frac{c_p^{HT}}{T'} dT' & T_f \leq T \end{cases} \tag{2}$$

Between the reference temperature, T_0 and the starting temperature of the transition, T_i, the contribution from the heat capacity of the low temperature phase is accounted for. During the phase transition, between T_i and T_f, the change in heat capacity is accounted for by defining c_p as: $c_p = (1 - x)c_p^{LT} + xc_p^{HT}$. Here, x is obtained by renormalizing the isobaric entropy changes to values ranging from 0 to 1. Above T_f, the contribution from the heat capacity of the high temperature phase is accounted for. T_0 was set to 270 K for both [choline]$_2$CoCl$_4$ and [choline]$_2$ZnCl$_4$ and $S_{c_p}(T_0) = 0$. For [choline]$_2$CoCl$_4$, $c_p^{LT} = 1225(4)$ J kg^{-1} K^{-1} and $c_p^{HT} = 1326(4)$ J kg^{-1} K^{-1}. For [choline]$_2$ZnCl$_4$, $c_p^{LT} = 1181(4)$ J kg^{-1} K^{-1} and $c_p^{HT} = 1251(4)$ J kg^{-1} K^{-1}.

As the pressure-induced volume change of the material outside the phase transition region gives rise to an isothermal change in entropy, S_{c_p} is pressure dependent. To account for this, an elastic heating contribution,[51] ΔS_+, can be calculated using the Maxwell relation $(\partial V/\partial T)_P = -(\partial S/\partial P)_T$:

$$\Delta S_+(P_f - P_i) = -\int_{P_i}^{P_f} \left(\frac{\partial V}{\partial T}\right) dP \tag{3}$$

This equation can be simplified by the assuming that the thermal expansion coefficient, α, is independent of the pressure:

$$\Delta S_+ = -(\partial V/\partial T)_{P=0} \cdot \Delta P = -(V \cdot \alpha) \cdot \Delta P \tag{4}$$

Here, V is the volume, T is the temperature, ΔP is the driving pressure $(P_f - P_i)$ and α is the thermal expansion coefficient at ambient pressure $(\alpha = V^{-1}(\partial V/\partial T)_{P=0})$. The final c_p adjusted ΔS_{ib} curves were constructed by the addition of ΔS_+ (using the α of the LT phase) and S_{c_p} to ΔS_{ib} for all pressures.

2.1.5 Calculation of isothermal entropy changes. The pressure-induced isothermal entropy changes, ΔS_{it}, were calculated using the quasi-direct method:[50]

$$\Delta S_{it(P_0 \to P)}(T,P) = \Delta S_{ib,cooling}(T,P) - \Delta S_{ib,cooling}(T,P_0) \tag{5}$$

$$\Delta S_{it(P \to P_0)}(T,P) = \Delta S_{ib,heating}(T,P_0) - \Delta S_{ib,heating}(T,P) \tag{6}$$

Here, the difference between ΔS_{ib} at ambient (P_0) and raised pressures (P), obtained on cooling and heating, are used to calculate the ΔS_{it} on compression and decompression respectively. Reversible isothermal entropy changes, $\Delta S_{it,rev}$ were determined by the overlap method.[51] Here, $\Delta S_{it,rev}$ is taken as the minimum value of $|\Delta S_{it,cooling}|$ compared to $|\Delta S_{it,heating}|$ at a given pressure for all temperatures.

2.1.6 Calculation of adiabatic temperature changes. The adiabatic temperature changes are determined from the c_p adjusted isobaric entropy curves through the quasi-direct method.[50]

$$\Delta T_{ad(P_0 \to P)} = T(S,P)_{cooling} - T(S,P_0)_{cooling} \tag{7}$$

$$\Delta T_{ad(P \to P_0)} = T(S,P_0)_{heating} - T(S,P)_{heating} \tag{8}$$

Here, the (irreversible) adiabatic temperature change induced by the initial compression and decompression, $\Delta T_{ad(P_0 \to P)}$ and $\Delta T_{ad(P \to P_0)}$ respectively, are calculated. The reversible adiabatic temperature changes, $\Delta T_{ad,rev}$, are calculated by the subtraction method where the difference is taken of the adiabatic temperature change curves obtained on cooling (at applied pressure) and on heating (ambient pressure):

$$\Delta T_{ad,rev} = T(S,P)_{cooling} - T(S,P_0)_{heating} \tag{9}$$

In this method $\Delta T_{ad,rev}$ is only obtained at pressures high enough to overcome the thermal hysteresis. Illustrated in Fig. 1f, under these conditions the difference between the ΔS_{ib} curves obtained on cooling (at pressure) and heating (at

ambient) is positive. Physically this implies the subtraction method only takes into account complete phase transitions[21] in contrast to the overlap method employed for the calculation of the reversible isothermal entropy changes which takes into account partial phase transitions as well.

2.1.7 Variable-temperature single crystal X-ray diffraction. Variable-temperature single crystal X-ray diffraction measurements were performed on cooling using a Bruker D8 Venture diffractometer equipped with a Photon 100 CMOS detector operating with Mo Kα radiation between 320 K to 100 K. The SAINT[52] routine as implemented in the Bruker APEX 4 (ref. 53) software package was used for data integration. Multi-scan absorption correction was performed using SADABS[54] for the untwinned data sets and TWINABS[55] for twinned data sets ($T <$ 290 K). For [choline]$_2$ZnCl$_4$ ($T \leq$ 250 K), the final datasets used for refinement were obtained by merging data from data collections on two different crystals to obtain properly scaled strong low-angle reflections. Final structure refinements and structure visualization were performed in Olex2.[56] For the monoclinic phase, the atomic displacement parameters (ADPs) of all non-hydrogen atoms were refined anisotropically. The ADPs of disordered atoms that are equivalent were restrained to be equal. For the orthorhombic phase, N–C, C–C and C–O bond distance restraints and equal ADP constraints were employed. To maintain a good data/parameter ratio, only the ADPs of the Co and Cl atoms were refined anisotropically. The X-ray crystallographic coordinates for structures reported in this study have been deposited at the Cambridge Crystallographic Data Centre (CCDC), under deposition numbers 2405717–2405731.

2.1.8 Variable-temperature-variable-pressure powder X-ray diffraction. Variable pressure powder X-ray diffraction experiments were performed up to 100 MPa at the Swiss-Norwegian BM01 beamline at the ESRF.[57] For the experiments at BM01, a glass capillary (outer diameter of 0.5 mm) was loaded with the powder sample and subsequently placed in a modified sapphire capillary cell.[58] Fluorinert FC-70 was added as the pressure transmitting medium and the sapphire cell was sealed with wax. A hydraulic pump was used to apply pressures of up to 100 MPa. A cryostream from Oxford cryosystems was used to vary the temperature. Due to thermal lag between the temperature of the cryostream and the temperature inside the capillary, a temperature calibration was performed on Ag powder, whereby the unit cell parameters were fitted to determine the temperature inside the capillary.[59]

For the patterns collected at 287.8 K between 10–50 MPa, Rietveld refinements were performed using Jana2020.[60] The remainder of the powder diffraction patterns were refined using cyclical Le Bail refinements in Jana2020.[60] The crystal structures from single crystal X-ray diffraction were used as starting points for the Rietveld refinements of both the monoclinic and orthorhombic phase. Due to a decrease in the data-to-parameter ratio compared to the SCXRD experiments, the crystallographic models were simplified before refinement. For the Rietveld refinement of the monoclinic phase, the disordered component was omitted. For both the orthorhombic and monoclinic phase the atomic displacement parameters were refined isotropically and both symmetry inequivalent cholines were refined as rigid

bodies. Additionally, constraints were used to set the ADPs of atoms of the same type to be identical to each other. Co–Cl and Cl–Cl bond distance restraints were employed. We note that the synchrotron radiation induces significant radiation damage in the samples and to combat this, the sample was moved between measurements.

2.2 Computational details

2.2.1 *Ab initio* molecular dynamics. *Ab initio* MD simulations were performed to investigate the structural dynamics of the two phases in [choline]$_2$CoCl$_4$ and [choline]$_2$ZnCl$_4$. These simulations were conducted under NVT conditions at T = 250 K and T = 340 K for [choline]$_2$CoCl$_4$ and at T = 250 K and T = 315 K for [choline]$_2$ZnCl$_4$ to represent the monoclinic ($P2_1/c$) and orthorhombic ($Pmcn$) phases using the CP2K package.[61] The simulations of the unit cell were performed with each unit cell comprising of 4 formula units, *i.e.* 8 cholines and 4 MCl$_4$$^{2-}$ (M = Co, Zn). The hybrid Gaussian and augmented plane wave method (GAPW), as implemented in the quickstep module of the CP2K package, was employed.[62] The calculation of ionic forces were performed using first-principles density functional theory. The dispersion interactions were included using the Grimme's DFT-D3 scheme,[63] and the Kohn–Sham orbitals of valence electrons were expanded in a Gaussian basis set (DZVP-MOLOPT for Co, Zn, Cl, C, N, O and H).[64] The dual-space GTH pseudopotentials[65–67] were used to take into account the effect of the core electrons. Spin-polarization was taken into account for Co^{2+} ions which were initialized in high spin configurations and collinear spin arrangement. The functional minimization was performed using the orbital transformation method.[68,69] A time step of 0.55 fs was employed to take into account the dynamics of the H atoms. The canonical sampling through velocity rescaling (CSVR) thermostat[70] was employed, with a small time constant of 10 fs for the initial equilibration steps for the $P2_1/c$ phase (∼2000 steps) and the $Pmcn$ phase (∼3500 steps) for [choline]$_2$CoCl$_4$ and ∼8000 steps for both the phases of [choline]$_2$ZnCl$_4$. A larger time constant of 100 fs was employed for the thermostat for the rest of the equilibration and production stages. The production simulations were performed for approximately 60 ps for [choline]$_2$CoCl$_4$ (for both phases) and 160 ps for [choline]$_2$ZnCl$_4$ (for both phases). The input files for the simulations are available in a public repository.[71] The vibrational spectra were calculated from the *ab initio* MD trajectories using TRAVIS.[72–74]

2.2.2 Hydrogen bonding analysis. The two distinct hydrogen bonding interactions present in this system, OH⋯Cl (choline-metallate) and OH⋯O (inter-choline) were modelled by defining a bond cutoff (∼2.5 Å for OH⋯Cl bond and 2.792 Å for OH⋯O bond) and an angular cutoff to take into account the directionality of hydrogen bond ($\angle$OHCl > 140° and $\angle$OHO > 110° (ref. 75 and 76)). The cutoffs applied here are relaxed compared to the rigid hydrogen bonding distances and angles in order to capture the dynamic hydrogen bonding present in this system.

2.2.3 Vibrational entropy. The long *ab initio* MD trajectories allow us to calculate the thermodynamic properties, such as

vibrational contribution to entropy change. The vibrational density of states (VDOS) can be calculated from the MD simulations using TRAVIS.[72–74] VDOS can be computed from the Fourier transform of the atomic velocity autocorrelation function (VACF). The VACF is defined as:

$$\text{VACF}(t) = \frac{1}{N} \sum_{i=1}^{N} \langle v_i(t) \cdot v_i(t+\tau) \rangle \quad (10)$$

where $v_i(t)$ is the velocity of atom i at time t, $v_i(t+\tau)$ is the velocity of atom i at a later time $t+\tau$ and $\langle \ldots \rangle$ is the statistical average in the NVT ensemble. The VDOS is expressed as:

$$g(\nu) = \int_0^\infty \text{VACF}(t) e^{i\nu t} dt \quad (11)$$

and is renormalized to $3N$, N being the number of atoms.

$$\int_0^\infty g(\nu) d\nu = 3N \quad (12)$$

The vibrational contribution to the entropy change is calculated as:

$$S(\nu) = -k_B \sum_{\nu=0}^{\nu_{\max}} \left[g(\nu) \left(\ln\left(1 - e^{h\nu/k_B T}\right) \right) + \frac{h\nu}{k_B T} \frac{1}{(1 - e^{h\nu/k_B T})} \right] \quad (13)$$

where $g(\nu)$ is the VDOS at frequency ν, k_B is Boltzmann constant, h being Planck constant and T is the temperature of the simulation. The vibrational contributions to entropy change are inherently inclusive of the temperature and anharmonic effects, which are vital to hybrid systems and determine the relative phase stability.[47,77]

3   Results and discussion

3.1   Barocaloric properties

The barocaloric effect is characterized by the isothermal entropy change, ΔS_{it}, and adiabatic temperature change, ΔT_{ad}, of a material under an applied pressure. To determine the barocaloric properties of [choline]$_2$CoCl$_4$ (Fig. 1a), differential scanning calorimetry (DSC) measurements are performed under applied pressures of 0.1–100 MPa around room temperature (277–323 K). Fig. 1b shows isobaric DSC traces of [choline]$_2$CoCl$_4$ collected on heating (positive heat flow) and cooling (negative heat flow). A single exothermic and endothermic peak is observed at $T = 287$ K and $T = 292$ K on cooling and heating respectively, which is indicative of a phase transition. The presence of thermal hysteresis with a width of ∼1 K (temperature difference between the onsets of the two phases) is consistent with a first-order phase transition. Shown in SI Fig. S1a and b, for [choline]$_2$CoCl$_4$ the isobaric entropy change associated with the phase transition, ΔS_{ib}, remains within 99% of the original value under applied pressures. For [choline]$_2$ZnCl$_4$ an increase of the ΔS_{ib} by 7% is observed from 0.1 MPa to 100 MPa (SI Fig. S2a and b). The evolution of ΔS_{it} with applied pressure is shown in Fig. 1c. The magnitude of ΔS_{it} increases with applied pressure, reaching a maximum value of 145 J kg^{-1} K^{-1} for $\Delta P = 100$ MPa. See methods section 2.1.5 for

details on the determination of ΔS_{it}, which includes both ambient-pressure heat capacities (SI Fig. S3a and b) and elastic heating contributions. From the overlap of the compression and decompression isothermal entropy curves, we determine the reversible isothermal entropy change, $\Delta S_{it,rev}$. From Fig. 1d it is apparent that with increasing pressure the $\Delta S_{it,rev}$ initially increases rapidly up to 60 MPa. Values of $\Delta S_{it,rev} \geq 100$ J kg^{-1} K^{-1} are reached for $\Delta P \geq 60$ MPa. $\Delta S_{it,rev}$ increases more slowly from 60 to 100 MPa and reaches a maximum value of 139 J kg^{-1} K^{-1} ($\Delta P = 100$ MPa). This behavior is reflected in the pressure dependence of the barocaloric strength, which is defined as the maximum entropy change normalized to the change in pressure.[50] Shown in SI Fig. S4, $\Delta S_{it,rev}/\Delta P$ shows a maximum of 1.73 J kg^{-1} K^{-1} MPa^{-1} for $\Delta P = 60$ MPa, which is comparable to some of the highest values for the barocaloric strength reported in the literature up to now.[78]

Using sufficiently long *ab initio* MD atomic trajectories (∼160 ps), the vibrational density of states (VDOS) were calculated for the monoclinic and orthorhombic phase of [choline]$_2$ZnCl$_4$ (SI Fig. S5). From the VDOS, the vibrational contribution to the entropy change was determined as $\Delta S_{vib} = S_{vib,315K} - S_{vib,250K} = 155(8)$ J kg^{-1} K^{-1} over a temperature difference of 65 K. This is in qualitative agreement with the experimental value for ΔS_{it}. See SI Note 1 and Fig. S7 for details of vibrational entropy calculation and error estimation. The vibrational contribution to the entropy change is dominated by the weak intermolecular interactions, such as hydrogen bonding interactions. As they are less stiff than purely ionic or covalent interactions they contribute to the plastic-like mechanical properties of the material.

We further calculate the orientational contribution to the entropy change arising from the reorientations of the choline cations in the monoclinic and orthorhombic phases of [choline]$_2$ZnCl$_4$ to be $\Delta S_{ori} = S_{ori,315K} - S_{ori,250K} = 3.4$ J K^{-1} kg^{-1}. ΔS_{ori} is an order of magnitude smaller than the ΔS_{vib} (∼2% of the vibrational entropy change), indicating that dominant contribution to the total entropy change is the ΔS_{vib}. See SI Note 2 and Fig. S9 for details of orientational entropy change calculations. We note that this value is comparable to the value reported for methylammonium PbI$_3$.[47]

From a materials design perspective, it is important that both the choline cations and the comparatively heavy MCl$_4^{2-}$ anions contribute to the vibrational entropy change. A key parameter governing the maximum temperature change accessible under a pressure swing is the ratio of the heat exchanged, Q, to the material's heat capacity, c_p (Q/c_p). This ratio is maximized by maximizing Q while minimizing c_p. Consequently, heavy ions such as MCl$_4^{2-}$, which significantly increase c_p, must not act as inert or "dead" thermal mass. Instead, both ions need to contribute actively to Q (proportional to ΔS_{it}) in order to maintain high cooling efficiency at the system level. The ion-decomposed VDOS for [choline]$_2$CoCl$_4$ and [choline]$_2$ZnCl$_4$ (SI Fig. S5) shows that the inorganic MCl$_4^{2-}$ (M = Co, Zn) anion contributes to the low frequency modes due to their relatively high atomic masses. The slow choline vibrations are spread throughout the spectrum, with the frequencies,
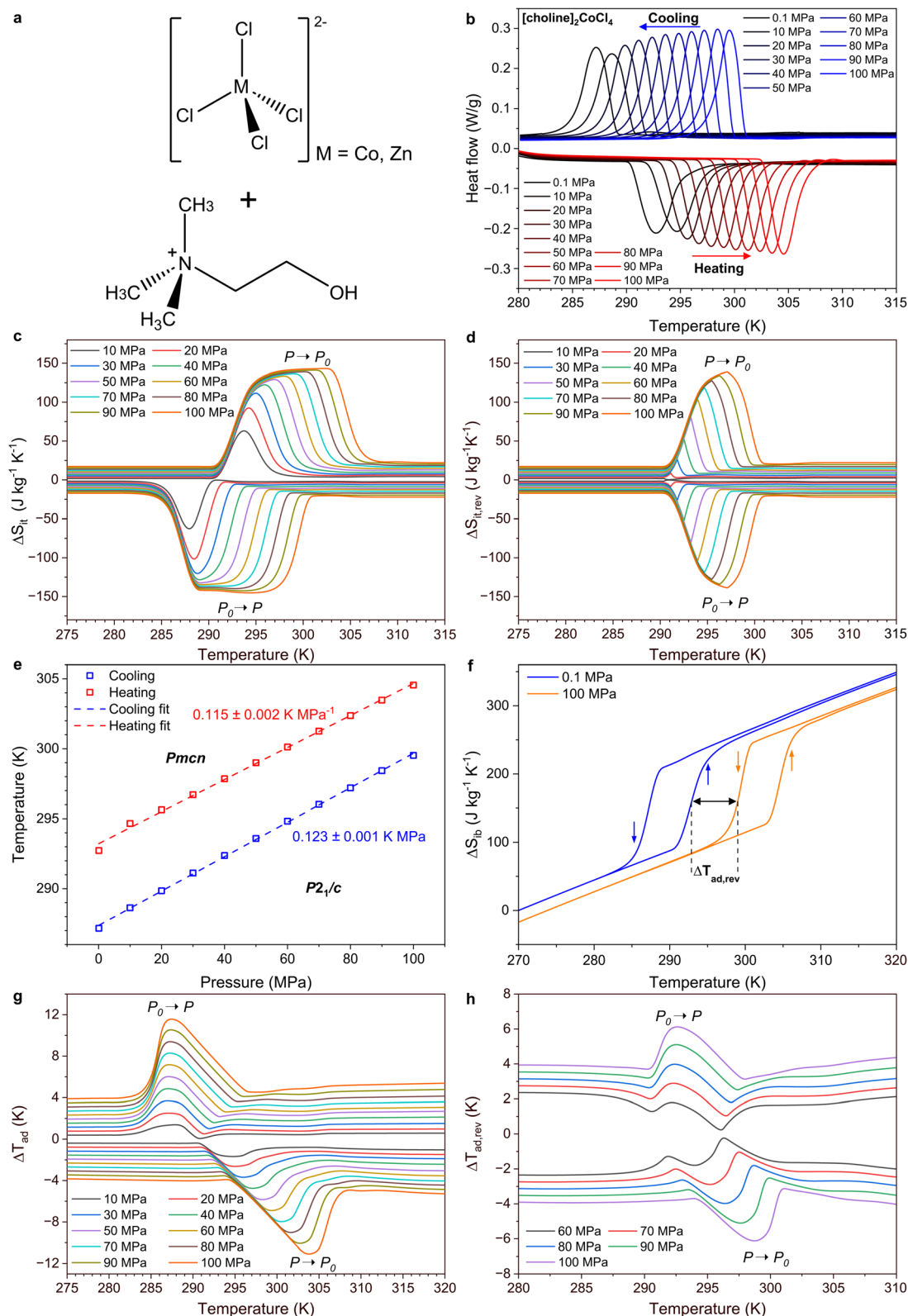
Fig. 1 Overview barocaloric properties [choline]$_2$CoCl$_4$. (a) Chemical structure of the MCl$_4^{2-}$ and choline ions. (b) Isobaric DSC traces of [choline]$_2$CoCl$_4$ collected on heating (negative heat flow) and cooling (positive heat flow). (c) Pressure-induced isothermal entropy changes (ΔS_{it}) for changes in pressures of 10 MPa to 100 MPa. (d) Reversible isothermal entropy changes ($\Delta S_{it,rev}$) for changes in pressures of 10 MPa to 100 MPa. (e) The evolution of the transition temperature (T_c is taken as the peak temperatures of (b)) against the applied pressure in MPa. The dashed lines correspond to linear fits of the data. The barocaloric coefficient (dT_c/dP) is denoted next to the data. (f) Heat capacity and elastic heating adjusted isobaric entropy changes (ΔS_{ib}) on heating and cooling determined for $P = 0.1$ MPa and 100 MPa. Here, the reversible adiabatic temperature change ($\Delta T_{ad,rev}$) is highlighted. (g) Adiabatic temperature changes (ΔT_{ad}) for changes in pressures of 10 MPa to 100 MPa. (h) Reversible adiabatic temperature changes ($\Delta T_{ad,rev}$) for changes in pressures of 10 MPa to 100 MPa.
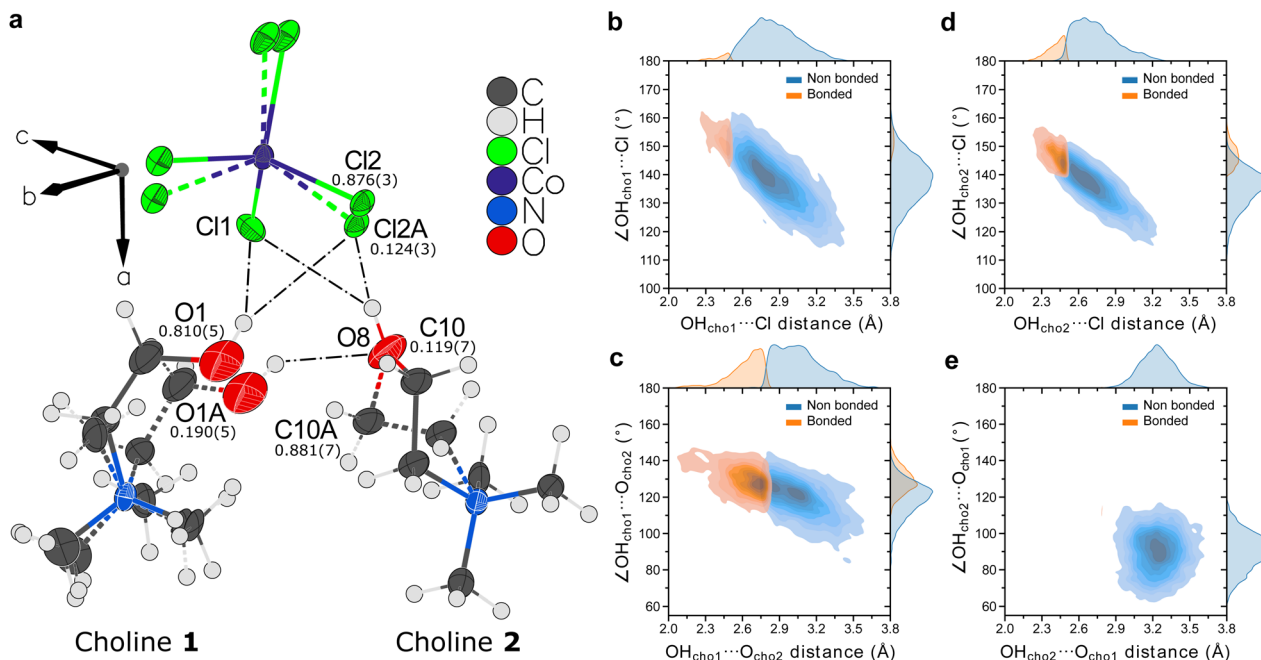
Fig. 2 Hydrogen bonding in the monoclinic phase. (a) Schematic of the hydrogen bonding and disorder present in the asymmetric unit of the monoclinic phase of [choline]$_2$CoCl$_4$ at 100 K. The thick dashed lines represent the bonds of the disordered parts and the dot-dashed lines represent the hydrogen bonds. The refined occupancies of the disordered parts are denoted below the corresponding atom label. The number in parentheses represents the estimated standard deviation. (b–e) Combined distribution functions of possible hydrogen bonds in the monoclinic phase that satisfy the geometric criteria of a hydrogen bond. The areas of high probability of hydrogen bonding are colored orange and areas of low probability, that do not satisfy the geometric criteria, are colored blue. The alternate axes show the distribution of the bonded and non bonded probabilities with orange and blue lines respectively. (b) Distribution of choline-CoCl$_4$$^{2-}$ (OH···Cl) hydrogen bonds involving choline **1**. (c) Distribution of inter-choline (OH···O) hydrogen bonds between choline **1** (donor) and choline **2** (acceptor). (d) Distribution of choline-CoCl$_4$$^{2-}$ (OH···Cl) hydrogen bonds involving choline **2**. (e) Distribution of inter-choline (OH···O) hydrogen bonds between choline **2** (donor) and choline **1** (acceptor).

$\nu < 300$ cm^{-1}, contributing to weak dispersion interactions between the choline and MCl$_4$$^{2-}$ (M = Co, Zn). Such soft modes persist in other hybrid materials such as CH$_3$NH$_3$PbI$_3$ and are responsible for the phase stability at high temperatures.[77] The vibrational contribution to the entropy change determined from the VDOS requires calculating ensemble averages over long simulation timescales, as the soft phonons ($\nu < 300$ cm^{-1}) present in [choline]$_2$ZnCl$_4$ struggle to converge at small simulation timescales (see SI Fig. S6–S8 and Note 1 for further details).

As expected for a conventional barocaloric, with increasing pressure the transition temperature, T_c (taken as the peak temperatures of Fig. 1b), shifts to higher temperatures. Shown in Fig. 1e, the barocaloric coefficient (dT_c/dP) can be extracted from the shift of T_c with pressure. Here, dT_c/dP has an average value of 0.119 K MPa^{-1}. The barocaloric coefficient illustrates the sensitivity of the transition to the applied pressure and in the case of [choline]$_2$CoCl$_4$ falls within the range typically observed for plastic crystals.[15,16,18] The construction of the ΔS_{ib} curves, shown for 0.1 and 100 MPa in Fig. 1f, allow for the determination of the expected (reversible) ΔT_{ad} with applied pressure. The pressure-induced ΔT_{ad}, shown in Fig. 1g shows a maximum of 11.6 K for $\Delta P = 100$ MPa. A maximum expected $\Delta T_{ad,max}$ of 33.5 K can be indirectly calculated through, $\Delta T_{ad} = -T\Delta S_{it}/c_p$. Through the subtraction method detailed in the

methods section, we determine the reversible adiabatic temperature change, $\Delta T_{ad,rev}$. Shown in Fig. 1h, ΔT_{ad} is fully reversible above $\Delta P > 60$ MPa and $\Delta T_{ad,rev}$ reaches a maximum of 6.1 K for $\Delta P = 100$ MPa. The $\Delta T_{ad,rev}$ is approximately half of the irreversible ΔT_{ad} and represents the magnitude of the temperature change one can expect in a refrigeration cycle.

In Fig. S10 of the SI an overview is given of the barocaloric properties of [choline]$_2$ZnCl$_4$. Compared to [choline]$_2$CoCl$_4$ smaller but comparable maximum values for ΔS_{it} and $\Delta S_{it,rev}$ of 130 J kg^{-1} K^{-1} and 128 J kg^{-1} K^{-1} are determined respectively for $\Delta P = 100$ MPa. Additionally, comparable maximum values for ΔT_{ad} and $\Delta T_{ad,rev}$ of 10.8 K and 6.1 K are determined respectively for $\Delta P = 100$ MPa. Near identical barocaloric coefficients of 0.117 K MPa^{-1} (heating) and 0.120 K MPa^{-1} (cooling) are determined for [choline]$_2$ZnCl$_4$.

The barocaloric properties of [choline]$_2$CoCl$_4$ and [choline]$_2$ZnCl$_4$ are tabulated in SI Table S1 alongside several best performing barocaloric materials from different material classes for $\Delta P \leq 100$ MPa. From SI Table S1 it is apparent that the $\Delta S_{it,rev}$ and $\Delta T_{ad,rev}$ of [choline]$_2$CoCl$_4$ and [choline]$_2$ZnCl$_4$ are competitive with other best-in-class hybrid ionic plastic crystals and perovskites. For $\Delta P \leq 100$ MPa, the classes of molecular plastic crystals and inorganic salts often exhibit no reversible entropy or temperature changes. Notable exceptions are C$_{60}$ ($\Delta T_{ad,rev} = 9$ K, $\Delta S_{it,rev} = 32$ J kg^{-1} K^{-1} (ref. 16)) and 1-Br-

Journal of Materials Chemistry A

adamantane ($\Delta T_{ad,rev} = 20$ K, $\Delta S_{it,rev} = 150$ J kg^{-1} K^{-1} (ref. 79)). Summarising, in a pressure range most crucial for future applications ($\Delta P \leq 100$ MPa), the barocaloric properties of [choline]$_2$CoCl$_4$ and [choline]$_2$ZnCl$_4$ are commensurate with other best-in-class barocaloric materials that exhibit structural order–disorder phase transitions.

3.2 Structural properties

Variable-temperature single crystal X-ray diffraction (VT-SCXRD) was performed between 100 K and 320 K to determine the crystal structures of [choline]$_2$CoCl$_4$ and [choline]$_2$ZnCl$_4$ and to follow their structural evolution with temperature. A structural phase transition is observed from a high-temperature orthorhombic phase (space group $Pmcn$) to a low-temperature monoclinic phase (space group $P2_1/c$) upon cooling below 290 K for both [choline]$_2$CoCl$_4$ and [choline]$_2$ZnCl$_4$. The phase transition coincides with the observed peak from the calorimetry measurements shown in Fig. 1b and SI S10a. The $h0l$ precession images that are constructed from data sets collected at 280 K and 290 K on [choline]$_2$CoCl$_4$ (shown in SI Fig. S11) clearly illustrate the change of crystal system over the phase transition. Note that [choline]$_2$CoCl$_4$ and [choline]$_2$ZnCl$_4$ are isostructural and therefore the following discussion on the structural properties of [choline]$_2$CoCl$_4$ is applicable to [choline]$_2$ZnCl$_4$ as well. The evolution of the (normalized) lattice parameters of [choline]$_2$CoCl$_4$ with temperature is plotted in SI Fig. S12. For both phases the thermal expansion is anisotropic. For $P2_1/c$, between 100–280 K, the b-axis expands by ~3% and is the largest contributor to the thermal expansion as the a- and c-axes only expand by roughly 1%. For $Pmcn$, between 290–320 K, the c-axis expands by 0.9% and is the dominant factor in the thermal expansion. On going through the phase transition, the unit cell volume increases by 2.4% ($\Delta V = 1.69 \times 10^{-5}$ m^3 kg^{-1}) discontinuously. The a-axis shrinks by 5.3% while the c- and b-axis expand by 6.3% and 0.4% respectively.

Besides the change in lattice symmetry, the precession images shown in SI Fig. S11 show that the phase transition is accompanied by non-merohedral twinning and the formation of two twin domains related by a 180° rotation around the [001] reciprocal lattice direction. Additionally, the resolution of the diffraction is significantly lower in the orthorhombic phase than in the monoclinic phase, consistent with the presence of structural disorder. Refinement of the phase fraction of the twin domains at 100 K yields a value of 0.3822(9) for the fraction of the second domain. The structure refinement parameters of the crystal structures of [choline]$_2$CoCl$_4$ and [choline]$_2$ZnCl$_4$ are detailed in SI Tables S2 and S3 for all temperatures. The fractional coordinates, equivalent isotropic displacement parameters, bond lengths, bond angles and refined atomic occupancies for the monoclinic (100 K) and orthorhombic (290 K) phases of [choline]$_2$CoCl$_4$ are tabulated in Tables S4–S11 in the SI.

The monoclinic and orthorhombic crystal structures are shown in SI Fig. S13a and S13b along the c-axis and a-axis respectively. The asymmetric unit and the hydrogen bonds involved in the monoclinic structure are highlighted in Fig. 2a. Two crystallographically distinct choline ions are identified. For

both ions, signs of disorder were apparent from the Fourier difference map and large oxygen ADPs. For choline **1**, a second orientation of the ion is identified (refined occupancy of 0.190(5) at 100 K). For choline **2**, the C atoms involved with the C–C bond are disordered (refined occupancy of 0.119(7) at 100 K). Furthermore, three of the four Cl atoms are also found to be disordered with their second sites close to the original position (refined occupancy of 0.124(3) at 100 K). For both orientations of choline **1**, the O–Cl1 distances are similar (O1–Cl1 = 3.537(6) Å and O1A–Cl1 = 3.51(2) Å) to the O8–Cl1 distance (3.481(4) Å) of choline **2**. The interatomic distances are slightly larger than the typical C$_{sp^3}$–OH···Cl hydrogen bond length of 3.10 Å.[75] Additionally, the O–Cl2A distances for choline **2** and the main orientation of choline **1**, O8–Cl2A = 2.971(11) Å and O1–Cl2A = 3.482(12) Å respectively, are close to the typical hydrogen bond length. This is in sharp contrast to the O1A–Cl2A distance of 3.78(2) Å for the second orientation of choline **1**. Besides OH··· Cl hydrogen bonding, possible inter-choline OH···O hydrogen bonding has to be taken into account. The inter-choline oxygen distance for the second orientation of choline **1**, O1A–O8 = 2.79(2) Å, is significantly shorter than the inter-choline oxygen distance of the main orientation, O1–O8 = 3.356(7) Å. The mean distance for C$_{sp^3}$–OH···C$_{sp^3}$–OH hydrogen bonds is 2.792(2) Å[76] and is in excellent agreement with the observed O1A–O8 distance. The interatomic distances suggest that the main orientations of choline **1** and choline **2** are able to form hydrogen bonds with either Cl1 or Cl2A while the second orientation of choline **1** is able to effectively form hydrogen bonds with choline **2**.

Using *ab initio* MD, we interpret the disorder observed in the crystallographic model of the monoclinic phase by analyzing the choline-metallate (OH···Cl) and inter-choline (OH···O) hydrogen bonds that are formed. The MD trajectories of the monoclinic phase (see SI Video, monoclinic.mpg in ref. 71) show two distinct choline ions, **1** and **2**, with different dynamic behaviors. The combined distribution plots (Fig. 2b–e) show areas of high and low probability of hydrogen bond formation, referred to as bonded and non bonded respectively. Choline **1** is able to form both inter-choline and choline-metallate hydrogen bonds (Fig. 2b and c), whereas choline **2** only forms choline-metallate hydrogen bonds (Fig. 2d and e). The OH···Cl bond formed by choline **1** is relatively weaker than the OH···Cl bond formed by choline **2**. Evidence for this is found in Fig. 2d, where a significantly higher probability, P, is observed for choline **2** compared to choline **1** (*i.e.* $P_{choline2}^{bonded}/P_{choline1}^{bonded} \sim 6$). This means choline **2** spends significantly more time in orientations where it is able to form hydrogen bonds to CoCl$_4^{2-}$ than choline **1**. The hydrogen bonding analysis is consistent with the two distinct cholines identified experimentally for the monoclinic phase. Additionally, the disorder observed experimentally can be interpreted as dynamic disorder where choline **1** dynamically switches between inter-choline and choline-metallate hydrogen bonds while choline **2** only forms choline-metallate hydrogen bonds.

For the orthorhombic phase, SCXRD reveals that two crystallographically inequivalent choline cations can be distinguished which are both found to be disordered across a mirror
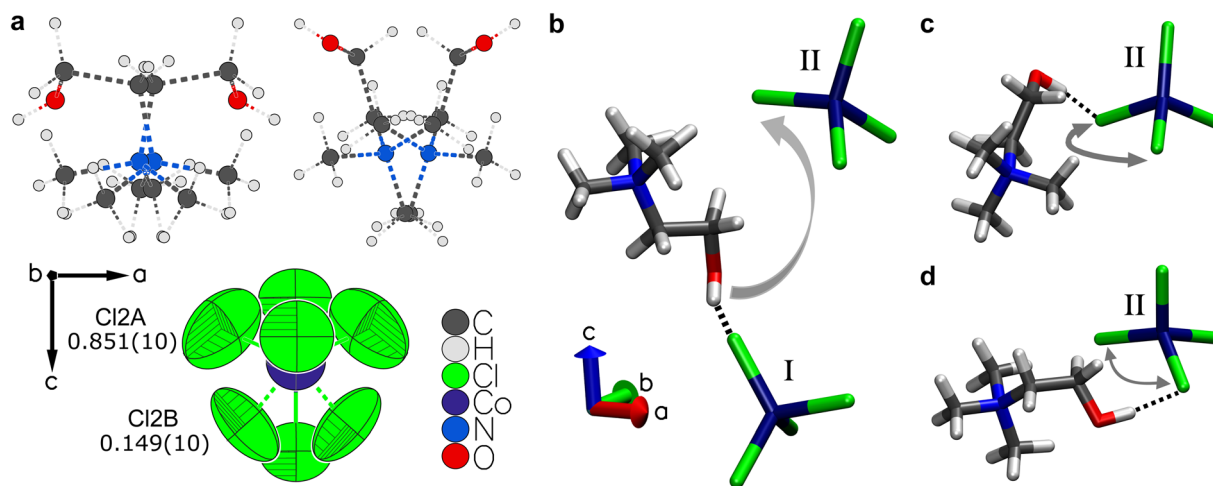
Fig. 3 Hydrogen bond dynamics in the orthorhombic phase. (a) Schematic of the crystallographic disorder present in the orthorhombic phase of [choline]$_2$CoCl$_4$ at 300 K. The dashed lines represent the bonds of the disordered parts. The refined occupancies of the disordered chlorine atoms are denoted below the corresponding atom label. The number in parentheses represents the estimated standard deviation. (b–d) Choline dynamics in the orthorhombic phase from *ab initio* MD simulations. (b) The OH⋯Cl hydrogen bond formed by choline switches between two inequivalent CoCl$_4^{2-}$ tetrahedra indicated by I and II. (c) Switching of the OH⋯Cl hydrogen bond between the chlorines of the same cobalt center (II) resulting in the configuration depicted in (d).

plane that lies in the ac-plane (Fig. 3a). Furthermore, the CoCl$_4^{2-}$ tetrahedron is found be to disordered as well. A single chlorine atom (Cl1 on Wyckoff site 4c) shows no sign of disorder suggesting the motion of the CoCl$_4^{2-}$ tetrahedron is not isotropic. The nature of the disorder for CoCl$_4^{2-}$ is highlighted in Fig. 3a. Here, it can be seen that the refined anisotropic displacement parameters for the chlorine atoms are large and the occupancy factors refine to a value of 0.851(10). X-ray diffraction yields a time and space average of the crystal structure and therefore the question whether the observed disorder in the orthorhombic structure is static or dynamic in nature requires an alternate approach.

Ab initio MD is used to interpret the hydrogen bonding which characterizes the orthorhombic phase. Compared to the monoclinic phase, choline-metallate hydrogen bonds are more prominent than the inter-choline hydrogen bonds. Two distinct types of dynamic behavior are observed for the set of choline-metallate (OH⋯Cl) interactions present in the orthorhombic phase: (a) inter-chloro metallate dynamics, where the OH⋯Cl bond switches between chlorine ions bonded to different metal centers (Fig. 3b) and (b) intra-chloro metallate dynamics, where the OH⋯Cl bond switches between chlorine ions bonded to the same metal centers (Fig. 3c and d). The inter-chloro metallate switching (Fig. 3b) is less probable than the intra-chloro metallate switching (Fig. 3c and d). This can be seen in the SI Video orthorhombic.mpg provided in the data repository.[71] For [choline]CoCl$_4$, inter-chloro metallate switching occurs roughly every ∼40–50 ps and is observed only for a subset of cholines. For [choline]ZnCl$_4$ however, most cholines show inter-chloro metallate switching which may indicate that [choline]ZnCl$_4$ exhibits a higher degree of dynamic disorder than [choline]CoCl$_4$. The large reorientations of the choline cations are consistent with the apparent disorder over a mirror plane seen in the crystallographic model.

We further calculate angular probability density functions describing the reorientations $f(\theta, \phi)$ of the choline cations. $f(\theta, \phi)$ is calculated from the time evolution of the polar (θ) and azimuthal (ϕ) angles with respect to the O–N vector of the choline ion. In the monoclinic phase (SI Fig. S9a), localized regions of high probability density (green color) are observed. This reflects the mostly static nature of the choline ions in the monoclinic phase and the absence of any large reorientations. In contrast, for the orthorhombic phase (SI Fig. S9b) the angular probability density is characterized by large diffuse regions with fewer localized regions of high probability density. This is consistent with the large reorientations exhibited by the choline cations in the orthorhombic phase.

3.3 Variable-pressure powder X-ray diffraction

To follow the evolution of the structure of [choline]$_2$CoCl$_4$ with applied pressure and to map its *P*–*T* phase diagram, isothermal powder X-ray diffraction experiments up to 100 MPa were performed at the Swiss-Norwegian BM01 beamline at the ESRF[57] between ∼287 K and ∼296 K with 2 MPa steps. Various heating and cooling protocols detailed in the methods section were employed to access different parts of the *P*–*T* phase space.

The evolution of the normalized lattice parameters with applied pressure are shown in Fig. 4a and b for the monoclinic (290 K) and orthorhombic (292.9 K) phase respectively. Additionally, the evolution of the lattice parameters with applied pressure are shown for the orthorhombic phase in SI Fig. S14 and the monoclinic phase in SI Fig. S15. Both phases exhibit a monotonic decrease of the unit cell lengths with increasing pressure. Over the 100 MPa pressure range their respective volumes change on the order of 1%. The pressure-induced changes in the lattice parameters shows that the compression is approximately isotropic, although a slight anisotropy is
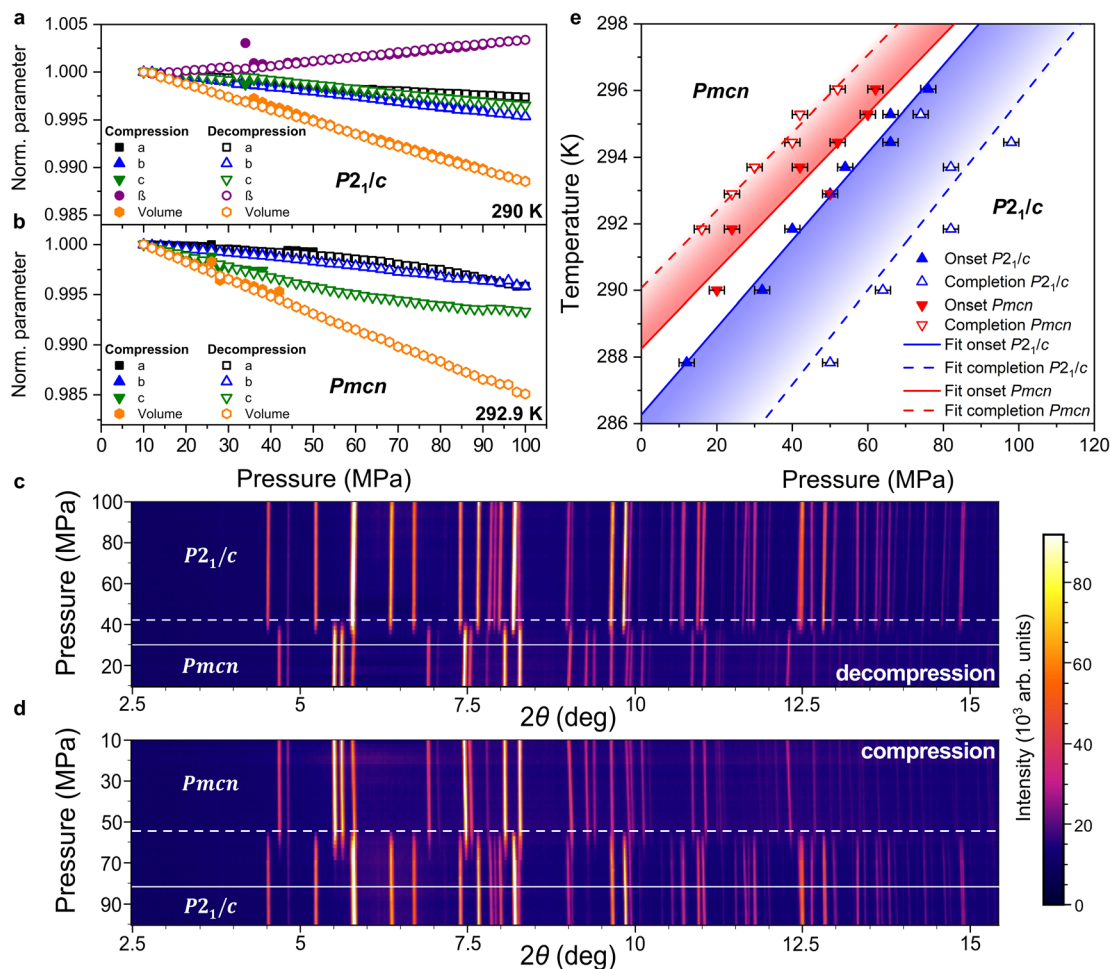
Fig. 4 Variable-pressure powder X-ray diffraction on [choline]$_2$CoCl$_4$. (a) Normalized lattice parameters for the monoclinic phase obtained from isothermal PXRD measurements performed at 290 K on compression (solid symbols) and decompression (open symbols) between 10 MPa and 100 MPa. (b) Normalized lattice parameters for the orthorhombic phase obtained from isothermal PXRD measurements performed at 292.9 K on compression (solid symbols) and decompression (open symbols) between 10 MPa and 100 MPa. (c and d) Waterfall plots of the isothermal PXRD measurements performed at 293.7 K ($\lambda = 0.66627$ Å) on decompression (c) and subsequent compression (d) between 10 MPa and 100 MPa. The intensities are colored according to the color bar next to the waterfall plots. The dashed lines indicate the onset of the phase transition and the solid lines indicate the completion of the phase transition. (e) Temperature–pressure phase diagram constructed from the onset and completion pressures of the phase transition determined from the isothermal PXRD measurements. The solid and open symbols represent the onset and completion pressures of the corresponding phase transition respectively. The solid and dashed lines indicate the linear fits to the onset and completion pressures of the corresponding phase transition respectively.

observed for the compression and decompression of the orthorhombic phase where the *c*-axis exhibits a larger maximum change (0.6%) compared to the other axes (0.4%). Visible more clearly in SI Fig. S14, a change in the slope is observed for the evolution of the *a*- and *c*-axis for the orthorhombic phase around 60 MPa, indicating a change of structural distortion mechanism. This behavior may originate from the anisotropic shape of the void space in the structure that is shown in SI Fig. S16. Shown in SI Fig. S17, isothermal bulk moduli of 5.783(16) GPa (*Pmcn*) and 7.497(18) GPa (*P2$_1$/c*) are determined from fits of pressure–volume data collected at 298 K and 290 K respectively, to second order Birch–Murnaghan equations of state.[80,81] The reduction of the bulk modulus on entering the *Pmcn* phase is consistent with the typical soft

mechanical properties of plastic crystalline phases that emerge from high degrees of dynamic structural disorder.[82]

The isothermal evolution of the diffraction patterns collected on cycling the applied pressure from 100 MPa to 10 MPa and back from 10 MPa to 100 MPa at 293.7 K is illustrated in Fig. 4c and d respectively. The sharp change of the diffraction patterns on both decompression and compression illustrates that the phase transition between the monoclinic (*P2$_1$/c*) and orthorhombic (*Pmcn*) phase can be driven reversibly with pressure. The phase coexistence region is highlighted with white lines in the figure. On decompression and compression, phase coexistence is observed over a 10 MPa and 18 MPa range respectively. Diffraction patterns inside and outside the phase coexistence region can be successfully refined using the Rietveld method, yielding good fits to the experimental data. SI Fig. S18 shows

typical examples of Rietveld refined single-phase orthorhombic, mixed phase and single-phase monoclinic patterns collected at 10, 18 and 50 MPa (287.8 K) respectively alongside their statistical fit factors. The unit cell parameters for the remaining pressure and temperature points were determined by Le Bail profile fitting of the powder patterns. Overviews of the resulting pressure–volume plots and statistical fit factors are given in SI Fig. S19–S21. How the phase transition proceeds with pressure was monitored by Rietveld refinement for $T \simeq 288$ K and by integration of the -111 and 111 reflections for the monoclinic and orthorhombic phase respectively against the applied pressure (for $T \simeq 288$ K and all other temperatures). In SI Fig. S22 the quantitative phase fraction (from Rietveld) is superimposed on the integrated intensities. Generally an excellent agreement is observed between the two methods of following the phase transition with pressure. The onset of the monoclinic phase occurs at 12 MPa. Roughly 95% of the maximum intensity is reached at 24 MPa. The transition is completed, *i.e.* no intensity is observed for the orthorhombic phase, at 52 MPa. The onset and completion pressures of the phase transition were determined for all isothermal measurements and are summarized in the phase diagram shown in Fig. 4e. The phase diagram indicates that a pressure of 60 MPa is required around 290 K to drive the phase transition to completion. This is in excellent agreement with the 60 MPa required to obtain a fully reversible adiabatic temperature change (Fig. 1h). We note however that as 95% of the transition can be driven by roughly half the pressure required to drive the full transition, the majority of the entropy change will occur in this region. Therefore, the practical pressure region of interest might be smaller than what is suggested by the phase diagram. An overview of the normalized integrated intensity plots against pressure are given for all temperatures in SI Fig. S23. Linear fits were performed on the onset and completion pressures of the phase transition on compression and decompression. An average barocaloric coefficient dT/dP of 0.126 ± 0.013 K MPa^{-1} is determined, 6% larger than the barocaloric coefficient determined through calorimetry. The Clausius–Clapeyron relation, $dT/dP = \Delta V_{\text{tr}}/\Delta S$, predicts a barocaloric coefficient of 0.117 K MPa^{-1}, using $\Delta S = 145.3$ J kg^{-1} K^{-1} and $\Delta V_{\text{tr}} = 1.69 \times 10^{-5}$ m^3 kg^{-1}. Additionally, from the average barocaloric coefficient determined from calorimetry of 0.119 K MPa^{-1}, an ΔS of 141.2 J kg^{-1} K^{-1} is predicted. The predicted values for the barocaloric coefficient and ΔS from the Clausius–Clapeyron relation are within 3% of the values determined from calorimetry.

Additionally, the variable-pressure powder and variable-temperature single crystal diffraction experiments presented above allow for the estimation of the volumetric contribution to the entropy change for [choline]$_2$CoCl$_4$ using $\Delta S_{\text{V}} = (\alpha/\kappa) \cdot \Delta V_{\text{tr}}$. Here, α is the thermal expansion coefficient at ambient pressure, κ is the isothermal compressibility and ΔV_{tr} is the change in specific volume over the phase transition at ambient pressure. The isothermal compressibility of the monoclinic phase at 290 K, $\kappa = V^{-1}(dV/dP)_T = 130.275 \pm 0.446$ TPa^{-1} and the thermal expansion coefficient at ambient pressure, $\alpha = V^{-1}(dV/dT)_P = 213.609 \pm 8.092$ MK^{-1}, were calculated using the PASCal tool.[83] With $\Delta V_{\text{tr}} = 1.69 \times 10^{-5}$ m^3 kg^{-1}, an ΔS_{V} of 27.77 ± 1.06 J kg^{-1} K^{-1}

is estimated. The volumetric contribution to the entropy change accounts for ∼19% of the total ΔS_{it}. Although this is a significant contribution it is apparent that the vibrational component to ΔS_{it} is the major driving force behind the barocaloric response of [choline]$_2$CoCl$_4$. This is consistent with the calculation of ΔS_{vib} from the *ab initio* MD simulations.

4 Conclusion and outlook

In this work, we present a thorough experimental and theoretical investigation into the barocaloric and structural properties of two isostructural members of the choline-based hybrid IPCs, [choline]$_2$CoCl$_4$ and [choline]$_2$ZnCl$_4$. Pressure-variable calorimetry measurements reveal a $\Delta S_{\text{it,rev}}$ around room temperature of 139 J kg^{-1} K^{-1} and 128 J kg^{-1} K^{-1} for [choline]$_2$CoCl$_4$ and [choline]$_2$ZnCl$_4$ respectively, for $\Delta P = 100$ MPa. Additionally, [choline]$_2$CoCl$_4$ and [choline]$_2$ZnCl$_4$ show a maximum reversible adiabatic temperature change, $\Delta T_{\text{ad,rev}}$, of 6.1 K for $\Delta P = 100$ MPa. For relatively small changes in pressure of $\Delta P \leq 100$ MPa, the barocaloric properties of [choline]$_2$CoCl$_4$ and [choline]$_2$ZnCl$_4$ are commensurate with other best-in-class barocaloric materials. The barocaloric response in this system originates mainly from the change in vibrational entropy across the order-disorder structural phase transition. This is evidenced by the calculated ΔS_{vib} from the estimated VDOS ($\Delta S_{\text{vib}} = 155(8)$ J kg^{-1} K^{-1} over the temperature range of 65 K), which is in qualitative agreement with the experimentally determined ΔS_{it}. Additionally, the estimated ΔS_{V} from X-ray diffraction experiments is ∼19% of the total ΔS_{it}.

The microscopic mechanism of the entropy change and the role of the choline ions herein are studied *via* a combination of SCXRD experiments and *ab initio* MD simulations. *Ab initio* MD and SCXRD experiments show that the ordered monoclinic phase is characterized by hydrogen bond frustration-driven dynamic disorder through the presence of various possible inter-choline and choline-CoCl$_4{}^{2-}$ hydrogen bond pathways. The heavy disorder observed experimentally in the disordered orthorhombic phase is also found to be dynamic in nature and manifests itself in the form of large reorientations of the choline ions, which form hydrogen bonds with different, spatially well separated, CoCl$_4{}^{2-}$ tetrahedra. The ion-decomposed VDOS shows that both choline and MCl$_4{}^{2-}$ ions contribute to the vibrational entropy change. *Via* pressure- and temperature-variable PXRD, the evolution of the phase transition in [choline]$_2$CoCl$_4$ is followed and a phase diagram is constructed. A good agreement is observed between the two experimental techniques which is reflected by the excellent agreement between the barocaloric coefficients determined through either technique. The excellent barocaloric properties of choline-based IPCs and the central role hydrogen bonding plays herein provides great promise for future studies. Taking inspiration from the known literature,[84–87] as the Zn and Co-based crystals are shown to be isostructural with near-identical barocaloric responses, this system will provide a fruitful platform to systematically explore the effect of halide substitution with Br$^-$ or I$^-$ on the barocaloric properties. Fundamentally weakening the hydrogen bond and introducing compositional

disorder may offer an effective route to tune the transition entropies, phase transition temperatures and the magnitude of the thermal hysteresis. As a result, a finer understanding of what drives the barocaloric properties of hybrid IPCs can be gained, leading to an understanding of how the barocaloric response can be tuned.

Author contributions

Conflicts of interest

There are no conflicts to declare.

Data availability

CCDC 2405717–2405731 contain the supplementary crystallographic data for this paper.[88a-o]

The data that support the findings of this study are available from the GitHub repository at https://github.com/hobdaylab/choline_based_plastic_crystals and the supplementary information (SI). Supplementary information is available. See DOI: https://doi.org/10.1039/d5ta05423k.

Acknowledgements

Notes and references

1 M. O. McLinden, J. S. Brown, R. Brignoli, A. F. Kazakov and P. A. Domanski, *Nat. Commun.*, 2017, **8**, 14476.

2 C. Aprea, A. Greco, A. Maiorino and C. Masselli, *Energy*, 2020, **190**, 116404.

3 H. Hou, S. Qian and I. Takeuchi, *Nat. Rev. Mater.*, 2022, **7**, 633–652.

4 B. Beckmann, L. Pfeuffer, J. Lill, B. Eggert, D. Koch, B. Lavina, J. Zhao, T. Toellner, E. E. Alp, K. Ollefs, K. P. Skokov, H. Wende and O. Gutfleisch, *ACS Appl. Mater. Interfaces*, 2024, **16**, 38208–38220.

5 P. Z. Z. Nehan, O. Vitayaya, D. R. Munazat, M. T. Manawan, D. Darminto and B. Kurniawan, *Phys. Chem. Chem. Phys.*, 2024, **26**, 14476–14504.

6 Z. Wang, H. Hou, H. Xue, Z. Ji, H. Zhang and X. Wang, *J. Mater. Chem. C*, 2025, **13**, 18009–18030.

7 A. Chauhan, S. Patel, R. Vaish and C. R. Bowen, *MRS Energy Sustain.*, 2015, **2**, 16.

8 Y. Sun, S. An, Y. Gao, Z. Yu, X. Yuan, Z. Ma, K. Shi, F. Hu and C. Wang, *J. Mater. Chem. A*, 2025, **13**, 6152–6175.

9 D. Boldrin, *Appl. Phys. Lett.*, 2021, **118**, 170502.

10 M. McLinden, *ASHRAE Handbook: Fundamentals*, ASHRAE, Atlanta, 2009.

11 J. Garcáa-Ben, I. Delgado-Ferreiro, J. Salgado-Beceiro and J. M. Bermúdez-Garcáa, *Barocaloric Effects in the Solid State*, IOP Publishing, 2023, pp. 6-1–6-35.

12 J. Garcáa-Ben, J. M. Bermúdez-Garcáa, R. J. Dixey, I. Delgado-Ferreiro, A. L. Llamas-Saiz, J. López-Beceiro, R. Artiaga, A. Garcáa-Fernández, U. B. Cappel, B. Alonso, S. Castro-Garcáa, A. E. Phillips, M. Sánchez-Andújar and M. A. Señarás-Rodráguez, *J. Mater. Chem. A*, 2023, **11**, 22232–22247.

13 J. Seo, R. Ukani, J. Zheng, J. D. Braun, S. Wang, F. E. Chen, H. K. Kim, S. Zhang, C. Thai, R. D. McGillicuddy, H. Yan, J. J. Vlassak and J. A. Mason, *J. Am. Chem. Soc.*, 2024, **146**, 2736–2747.

14 P. Lloveras, A. Aznar, M. Barrio, P. Negrier, C. Popescu, A. Planes, L. Mañosa, E. Stern-Taulats, A. Avramenko, N. D. Mathur, X. Moya and J. L. Tamarit, *Nat. Commun.*, 2019, **10**, 1803.

15 A. Aznar, P. Lloveras, M. Barrio, P. Negrier, A. Planes, L. Mañosa, N. D. Mathur, X. Moya and J. L. Tamarit, *J. Mater. Chem. A*, 2020, **8**, 639–647.

16 J. Li, D. Dunstan, X. Lou, A. Planes, L. Mañosa, M. Barrio, J. L. Tamarit and P. Lloveras, *J. Mater. Chem. A*, 2020, **8**, 20354–20362.

17 S. L. Piper, L. Melag, M. Kar, A. Sourjah, X. Xiao, E. F. May, K.-F. Aguey-Zinsou, D. R. MacFarlane and J. M. Pringle, *Science*, 2025, **387**, 56–62.

18 P. Dafonte-Rodriguez, I. Delgado-Ferreiro, J. Garcia-Ben, A. Ferradanes-Martinez, M. Gelpi, J. Walker, C. J. McMonagle, S. Castro-Garcia, M. A. Senaris-Rodriguez, J. M. Bermudez-Garcia and M. Sánchez-Andujar, *Chem. Commun.*, 2024, **60**, 14065–14068.

19 Y.-H. Gao, D.-H. Wang, F.-X. Hu, Q.-Z. Huang, Y.-T. Song, S.-K. Yuan, Z.-Y. Tian, B.-J. Wang, Z.-B. Yu, H.-B. Zhou, Y. Kan, Y. Lin, J. Wang, Y.-L. Li, Y. Liu, Y.-Z. Chen, J.-R. Sun, T.-Y. Zhao and B.-G. Shen, *Nat. Commun.*, 2024, **15**, 1838.

20 Y. Gao, H. Liu, F. Hu, H. Song, H. Zhang, J. Hao, X. Liu, Z. Yu, F. Shen, Y. Wang, H. Zhou, B. Wang, Z. Tian, Y. Lin, C. Zhang, Z. Yin, J. Wang, Y. Chen, Y. Li, Y. Song, Y. Shi, T. Zhao, J. Sun, Q. Huang and B. Shen, *NPG Asia Mater.*, 2022, **14**, 34.

21 J. Seo, R. D. McGillicuddy, A. H. Slavney, S. Zhang, R. Ukani, A. A. Yakovenko, S. L. Zheng and J. A. Mason, *Nat. Commun.*, 2022, **13**, 2536.

22 S. P. Vallone, A. N. Tantillo, A. M. dos Santos, J. J. Molaison, R. Kulmaczewski, A. Chapoy, P. Ahmadi, M. A. Halcrow and K. G. Sandeman, *Adv. Mater.*, 2019, **31**, 1807334.

23 M. Romanini, Y. X. Wang, K. Gürpinar, G. Ornelas, P. Lloveras, Y. Zhang, W. Zheng, M. Barrio, A. Aznar, A. GrÃ cia-Condal, B. Emre, O. Atakol, C. Popescu, H. Zhang, Y. Long, L. Balicas, J. L. Tamarit, A. Planes, M. Shatruk and L. Mañosa, *Adv. Mater.*, 2021, **33**, 2008076.

24 K. Lünser, E. Kavak, K. Gürpinar, B. Emre, O. Atakol, E. Stern-Taulats, M. Porta, A. Planes, P. Lloveras, J.-L. Tamarit and L. Mañosa, *Nat. Commun.*, 2024, **15**, 6171.

25 Z. Zhang, X. Jiang, T. Hattori, X. Xu, M. Li, C. Yu, Z. Zhang, D. Yu, R. Mole, S.-I. Yano, J. Chen, L. He, C.-W. Wang, H. Wang, B. Li and Z. Zhang, *Mater. Horiz.*, 2023, **10**, 977–982.

26 J. Timmermans, *J. Chem. Phys.*, 1938, **35**, 331–344.

27 J. H. Lee, J. H. Lee, E. H. Kong and H. M. Jang, *Sci. Rep.*, 2016, **6**, 21687.

28 J. H. Lee, N. C. Bristowe, P. D. Bristowe and A. K. Cheetham, *Chem. Commun.*, 2015, **51**, 6434–6437.

29 F. B. Li, M. Li, X. Xu, Z. C. Yang, H. Xu, C. K. Jia, K. Li, J. He, B. Li and H. Wang, *Nat. Commun.*, 2020, **11**, 4190.

30 I. De Pedro, A. García-Saiz, J. González, I. Ruiz De Larramendi, T. Rojo, C. A. Afonso, S. P. Simeonov, J. C. Waerenborgh, J. A. Blanco, B. Ramajo and J. R. Fernández, *Phys. Chem. Chem. Phys.*, 2013, **15**, 12724–12733.

31 S. H. Zeisel and K. A. Da Costa, *Nutr. Rev.*, 2009, **67**, 615–623.

32 H. Zhu, D. R. MacFarlane, J. M. Pringle and M. Forsyth, *Trends Chem.*, 2019, **1**, 126–140.

33 P. De Vreese, N. R. Brooks, K. Van Hecke, L. Van Meervelt, E. Matthijs, K. Binnemans and R. Van Deun, *Inorg. Chem.*, 2012, **51**, 4972–4981.

34 A. Bayu, A. Yoshida, S. Karnjanakom, K. Kusakabe, X. Hao, T. Prakoso, A. Abudula and G. Guan, *Green Chem.*, 2018, **20**, 4112–4119.

35 L. Jin, K. M. Nairn, C. M. Forsyth, A. J. Seeber, D. R. MacFarlane, P. C. Howlett, M. Forsyth and J. M. Pringle, *J. Am. Chem. Soc.*, 2012, **134**, 9688–9697.

36 D. Chandra, C. S. Day and C. S. Barrett, *Powder Diffr.*, 1993, **8**, 109–117.

37 D. G. Bounds, M. L. Klein and G. N. Patey, *J. Chem. Phys.*, 1980, **72**, 5348–5356.

38 G. S. Pawley, *Mol. Phys.*, 1981, **43**, 1321–1330.

39 I. R. McDonald, D. G. Bounds and M. L. Klein, *Mol. Phys.*, 1982, **45**, 521–542.

40 M. Forsyth, F. Chen, L. A. O'Dell and K. Romanenko, *Solid State Ionics*, 2016, **288**, 160–166.

41 N. Sirigiri, F. Chen, C. M. Forsyth, R. Yunis, L. O'Dell, J. M. Pringle and M. Forsyth, *Mater. Today Phys.*, 2022, **22**, 100603.

42 F. Chen, L. Jin, S. W. De Leeuw, J. M. Pringle and M. Forsyth, *J. Chem. Phys.*, 2013, **138**, 244503.

43 M. Yoneya and J. Harada, *J. Phys. Chem. C*, 2020, **124**, 2171–2177.

44 J. B. Hooper and O. Borodin, *Phys. Chem. Chem. Phys.*, 2010, **12**, 4635–4643.

45 J. Adebahr, F. C. Grozema, S. W. deLeeuw, D. R. MacFarlane and M. Forsyth, *Solid State Ionics*, 2006, **177**, 2845–2850.

46 F. Li, M. Li, C. Niu and H. Wang, *Appl. Phys. Lett.*, 2022, **120**, 073902.

47 C. Escorihuela-Sayalero, L. C. Pardo, M. Romanini, N. Obrecht, S. Loehlé, P. Lloveras, J. Â. Tamarit and C. Cazorla, *npj Comput. Mater.*, 2024, **10**, 13.

48 K. Sau, T. Ikeshoji, S. Takagi, O. Shin-ichi, D. Errandonea and D. Chu, *Sci. Rep.*, 2021, **11**, 11915.

49 E. Palacios, J. J. Melero, R. Burriel and P. Ferloni, *Phys. Rev. B: Condens. Matter Mater. Phys.*, 1996, **54**, 9099–9108.

50 X. Moya, S. Kar-Narayan and N. D. Mathur, *Nat. Mater.*, 2014, **13**, 439–450.

51 X. Moya and N. D. Mathur, *Science*, 2020, **370**, 797–803.

52 Bruker, *SAINT*, Bruker AXS Inc., Madison, Wisconsin, USA, 2012.

53 Bruker, *APEXII*, Bruker AXS Inc., Madison, Wisconsin, USA, 2012.

54 Bruker, *SADABS*, Bruker AXS Inc., Madison, Wisconsin, USA, 2001.

55 G. Sheldrick, *TWINABS*, University of Göttingen, Göttingen, 2012.

56 O. V. Dolomanov, L. J. Bourhis, R. J. Gildea, J. A. Howard and H. Puschmann, *J. Appl. Crystallogr.*, 2009, **42**, 339–341.

57 V. Dyadkin, P. Pattison, V. Dmitriev and D. Chernyshov, *J. Synchrotron Radiat.*, 2016, **23**, 825–829.

58 C. J. McMonagle, D. R. Allan, M. R. Warren, K. V. Kamenev, G. F. Turner and S. A. Moggach, *J. Appl. Crystallogr.*, 2020, **53**, 1519–1523.

59 K. P. Marshall, H. Emerich, C. J. Mcmonagle, C. A. Fuller, V. Dyadkin, D. Chernyshov, W. Van Beek and K. Kvashnina, *J. Synchrotron Radiat.*, 2023, **30**, 267–272.

60 V. Petříček, L. Palatinus, J. Plášil and M. Dušek, *Z. Kristallogr.*, 2023, **238**, 271–282.

61 T. D. Kühne, M. Iannuzzi, M. Del Ben, V. V. Rybkin, P. Seewald, F. Stein, T. Laino, R. Z. Khaliullin, O. Schütt, F. Schiffmann, D. Golze, J. Wilhelm, S. Chulkov, M. H. Bani-Hashemian, V. Weber, U. Borštnik, M. Taillefumier, A. S. Jakobovits, A. Lazzaro and H. Pabst, *J. Chem. Phys.*, 2020, **152**, 194103.

62 J. VandeVondele, M. Krack, F. Mohamed, M. Parrinello, T. Chassaing and J. Hutter, *Comput. Phys. Commun.*, 2005, **167**, 103–128.

63 S. Grimme, J. Antony, S. Ehrlich and H. Krieg, *J. Chem. Phys.*, 2010, **132**, 154104.

64 J. VandeVondele and J. Hutter, *J. Chem. Phys.*, 2007, **127**, 114105.

65 S. Goedecker, M. Teter and J. Hutter, *Phys. Rev. B: Condens. Matter Mater. Phys.*, 1996, **54**, 1703–1710.

66 C. Hartwigsen, S. Goedecker and J. Hutter, *Phys. Rev. B: Condens. Matter Mater. Phys.*, 1998, **58**, 3641–3662.

67 M. Krack, *Theor. Chem. Acc.*, 2005, **114**, 145–152.

68 J. VandeVondele and J. Hutter, *J. Chem. Phys.*, 2003, **118**, 4365–4369.

69 V. Weber, J. VandeVondele, J. Hutter and A. M. N. Niklasson, *J. Chem. Phys.*, 2008, **128**, 084113.

70 G. Bussi, D. Donadio and M. Parrinello, *J. Chem. Phys.*, 2007, **126**, 014101.

71 *HobdayLab*, 2024, https://github.com/hobdaylab/choline_based_plastic_crystals.

72 M. Brehm, M. Thomas, S. Gehrke and B. Kirchner, *J. Chem. Phys.*, 2020, **152**, 164105.

73 M. Thomas, M. Brehm, R. Fligg, P. Vöhringer and B. Kirchner, *Phys. Chem. Chem. Phys.*, 2013, **15**, 6608–6622.

74 M. Brehm and B. Kirchner, *J. Chem. Inf. Model.*, 2011, **51**, 2007–2023.

75 T. Steiner, *Acta Crystallogr.*, 1998, **B54**, 456–463.

76 T. Steiner, *Angew. Chem., Int. Ed.*, 2002, **41**, 48–76.

77 K. T. Butler, K. Svane, G. Kieslich, A. K. Cheetham and A. Walsh, *Phys. Rev. B*, 2016, **94**, 180103.

78 Q. Ren, J. Qi, D. Yu, Z. Zhang, R. Song, W. Song, B. Yuan, T. Wang, W. Ren, Z. Zhang, X. Tong and B. Li, *Nat. Commun.*, 2022, **13**, 2293.

79 A. Aznar, P. Negrier, A. Planes, L. Mañosa, E. Stern-Taulats, X. Moya, M. Barrio, J.-L. Tamarit and P. Lloveras, *Appl. Mater. Today*, 2021, **23**, 101023.

80 F. Birch, *Phys. Rev.*, 1947, **71**, 809–824.

81 R. J. Angel, M. Alvaro and J. Gonzalez-Platas, *Z. Kristallogr. Cryst. Mater.*, 2014, **229**, 405–419.

82 S. Das, A. Mondal and C. M. Reddy, *Chem. Soc. Rev.*, 2020, **49**, 8878–8896.

83 M. Lertkiattrakul, M. L. Evans and M. J. Cliffe, *J. Open Source Softw.*, 2023, **8**, 5556.

84 J. García-Ben, M. Gelpi, P. Dafonte-Rodríguez, Á. Ferradanes-Martínez, I. Delgado-Ferreiro, J. López-Beceiro, R. Artiaga, A. L. Llamas-Saiz, J. Walker, C. J. McMonagle, A. García-Fernández, U. B. Cappel, S. Castro-García, M. A. Señarís-Rodríguez, J. M. Bermúdez-García and M. Sánchez-Andújar, *Inorg. Chem. Front.*, 2025, **12**, 7282–7293.

85 R. L. Kingsford, S. R. Jackson, L. C. Bloxham and C. G. Bischak, *J. Am. Chem. Soc.*, 2023, **145**, 11773–11780.

86 F. Li, C. Niu, X. Xu, M. Li and H. Wang, *Appl. Phys. Lett.*, 2022, **121**, 223902.

87 X. Xu, F. Li, C. Niu, M. Li and H. Wang, *Appl. Phys. Lett.*, 2023, **122**, 043901.

88 (*a*) CCDC 2405717: Experimental Crystal Structure Determination, 2025, DOI: 10.5517/ccdc.csd.cc2lrbsh; (*b*) CCDC 2405718: Experimental Crystal Structure Determination, 2025, DOI: 10.5517/ccdc.csd.cc2lrbtj; (*c*) CCDC 2405719: Experimental Crystal Structure Determination, 2025, DOI: 10.5517/ccdc.csd.cc2lrbvk; (*d*) CCDC 2405720: Experimental Crystal Structure Determination, 2025, DOI: 10.5517/ccdc.csd.cc2lrbwl; (*e*) CCDC 2405721: Experimental Crystal Structure Determination, 2025, DOI: 10.5517/ccdc.csd.cc2lrbxm; (*f*) CCDC 2405722: Experimental Crystal Structure Determination, 2025, DOI: 10.5517/ccdc.csd.cc2lrbyn; (*g*) CCDC 2405723: Experimental Crystal Structure Determination, 2025, DOI: 10.5517/ccdc.csd.cc2lrbzp; (*h*) CCDC 2405724: Experimental Crystal Structure Determination, 2025, DOI: 10.5517/ccdc.csd.cc2lrc0r; (*i*) CCDC 2405725: Experimental Crystal Structure Determination, 2025, DOI: 10.5517/ccdc.csd.cc2lrc1s; (*j*) CCDC 2405726: Experimental Crystal Structure Determination, 2025, DOI: 10.5517/ccdc.csd.cc2lrc2t; (*k*) CCDC 2405727: Experimental Crystal Structure Determination, 2025, DOI: 10.5517/ccdc.csd.cc2lrc3v; (*l*) CCDC 2405728: Experimental Crystal Structure Determination, 2025, DOI: 10.5517/ccdc.csd.cc2lrc4w; (*m*) CCDC 2405729: Experimental Crystal Structure Determination, 2025, DOI: 10.5517/ccdc.csd.cc2lrc5x; (*n*) CCDC 2405730: Experimental Crystal Structure Determination, 2025, DOI: 10.5517/ccdc.csd.cc2lrc6y; (*o*) CCDC 2405731: Experimental Crystal Structure Determination, 2025, DOI: 10.5517/ccdc.csd.cc2lrc7z.